Multiscale Simulation Performed on ISSP Super Computer:Analysis of Entangled Polymer Melt Flow

Takahiro Murashima
Department of Physics, Tohoku University
Aramaki-Aza-Aoba, Aoba-Ward, Sendai, Miyagi 980-8578

Abstract

Multiscale simulation of entangled polymer melt flow has been developed based on the smoothed particle hydrodynamics model and the dual slip-link model. A kernel gradient free method and a particle shifting method were implemented to improve the accuracy of the macroscopic fluid dynamics and stabilize the multiscale simulation. We have investigated an effect of the polymer chain length on the fluid dynamic behavior. Since the longer chain has the longer correlation time, the non-linearity in the macroscopic field is enhanced in the longer chain case.

1 Introduction

Flow prediction of polymer melt is important for industrial processing [1–3]. Microscopic polymer dynamics has a long correlation time between a past state and the current state, and the flow histories of polymer chain affect the macroscopic flow dynamics. The microscopic polymer dynamics should be considered to predict the macroscopic flow dynamics of polymer melt. It is, however, difficult to include the microscopic polymer dynamics into the macroscopic flow dynamics because there are large scale differences on space and time between microscopic polymer dynamics and the macroscopic flow dynamics.

Micro-macro bridging approaches have been done by several groups in two decades and they have succeeded to treat simple viscoelastic fluids without entanglements of polymer chains [4–10] and also with entanglements [11]. We have proposed a multiscale simulation technique to treat the entangled polymer melt flow using a different approach [12–15]. Our multiscale simulation is based on the fluid particle simulation and the coarse-grained entangled polymer dynamics simulation. Each fluid particle has a polymer simulator, where the states of polymer chains are different from those in the other fluid particles. At each position, the stress tensor $\boldsymbol{\sigma}$ is calculated from the polymer simulator in the fluid particle. The macroscopic flow field $\boldsymbol{v}$ is updated through the momentum balance equation, and then the velocity gradient tensor $\boldsymbol{\kappa} = (\boldsymbol{\nabla v})^{\mathrm{T}}$ is calculated at each fluid particle. Under the renewed velocity gradient tensor $\boldsymbol{\kappa}$, polymer dynamics simulation is performed and the stress tensor is renewed. The macroscopic states and the microscopic states are updated alternately in the multiscale simulation. This way is same with the heterogeneous multiscale method that the several time steps of molecular dynamics simulation fits to the one time step of fluid dynamics simulation [16–21].

To consider the flow history of polymer chain, the macroscopic fluid dynamics is solved using the fluid particle simulation. The smoothed particle hydrodynamics (SPH) method is widely used to simulate the fluid dynamics of simple liquids and polymer melts [22–28]. However, SPH is defective to calculating the spatial gradient of physical

variables near wall boundaries and surfaces. To correct the gradient of field variables in SPH, a corrective SPH method [29,30], a modified SPH (MSPH) method [31], and a finite particle method (FPM) [32] have been developed. These methods have succeeded in calculating the gradient of field variables more accurate than the original SPH method. Very recently, a kernel gradient free (KGF) method has been developed [33]. This new method does not need to calculate in literally the kernel gradient. KGF improves the gradient of field variables and KGF is more stable than MSPH and FPM. Since the spatial homogeneity of fluid particles affects the accuracy of fluid particle simulation, we use a particle shifting method (PSM) [34] to correct and distribute the fluid particles equally at every time steps. KGF and PSM improves the accuracy of the multiscale simulation.

The correlation time of entangled polymer chains with length ℓ is proportional to $\ell^{3.5}$ and is larger than of the order of milliseconds. Such a long time scale is not accessible with the conventional coarse-grained molecular dynamics simulation, so called Kremer-Grest model [35]. Based on the reptation theory with the some extensions [36–39], several entangled polymer dynamics simulators have been developed [40–47]. In our multiscale simulation, we use the dual slip-link model [44]. The merit to use the dual slip-link model is that the model can predict the rheological properties of the standard polymer chains, such as polyethylene and polystyrene, the algorithm is simple to simulate the entangled polymer dynamics, and the model does not require much computation time.

We investigate the effect of the polymer chain length to the macroscopic field. In the next section, we review the procedure of the multiscale simulation, the kernel gradient free method, the particle shifting method, and the dual slip-link model. Then, we discuss on the flow dynamics around a obstacle. This problem is same with the previous works [13, 15]. We discuss the effect of the polymer chain length difference using the revised multiscale simulation method.

2 Multiscale Simulation

The multiscale simulation is based on the fluid particle simulation and the polymer dynamics simulation. Polymer melt flow is described with the dynamics of fluid particle according to the following equations.

$$\frac{\mathrm{d}\boldsymbol{x}}{\mathrm{d}t} = \boldsymbol{v}, \tag{1}$$

$$\rho\frac{\mathrm{d}\boldsymbol{v}}{\mathrm{d}t} = \boldsymbol{\nabla}\cdot\boldsymbol{\sigma} + \rho\boldsymbol{g}, \tag{2}$$

where $\boldsymbol{x}$ is the position, $\boldsymbol{v}$ is the velocity, ρ is the density, $\boldsymbol{\sigma}$ is the stress tensor, and $\boldsymbol{g}$ is the external force. The density $\rho(\boldsymbol{x})$ is obtained using the kernel function $W(|\boldsymbol{x}' - \boldsymbol{x}|, h)$ to interpolate the particle $\boldsymbol{x}$ and the neighboring particles $\boldsymbol{x}'$,

$$\rho(\boldsymbol{x}) = \int \mathrm{d}\boldsymbol{x}' m W(|\boldsymbol{x}' - \boldsymbol{x}|, h), \tag{3}$$

where m is the mass of fluid particle. We use the following kernel function,

$$W(r,h) = \begin{cases} \frac{A_d}{(h\sqrt{\pi})^d}\left[e^{-r^2/h^2} - e^{-4}\right], & r \le 2h, \\ 0, & r > 2h, \end{cases} \tag{4}$$

where d is the dimension of the system, and the normalization coefficient A_d is calculated from $\int \mathrm{d}\boldsymbol{r} W(|\boldsymbol{r}|, h) = 1$, and found to be $A_1 = 1.04823$, $A_2 = 1.10081$ and $A_3 = 1.18516$. The half value of width of kernel function h is set to $1.5\delta_0$ where δ_0 is the initial distance between fluid particles. The stress tensor $\boldsymbol{\sigma}$ consists of the hydrostatic pressure term, the viscous stress term, and the polymeric stress term:

$$\boldsymbol{\sigma} = -p\boldsymbol{I} + \boldsymbol{\sigma}_\mathrm{s} + \boldsymbol{\sigma}_\mathrm{p}. \tag{5}$$

The hydrostatic pressure p is determined from the density deviation:

$$p - p_0 = C^2(\rho - \rho_0), \tag{6}$$

where C is the sound velocity, p_0 and ρ_0 are the reference pressure and density, respectively. The viscous stress coming from the molecular vibration ignored in the coarse grained polymer dynamics simulation is assumed to $\boldsymbol{\sigma}_{\mathrm{s}} = \eta_s \left\{ (\boldsymbol{\nabla} \boldsymbol{v})^{\mathrm{T}} + \boldsymbol{\nabla} \boldsymbol{v} \right\}$ where η_s the viscous constant. The polymeric stress $\boldsymbol{\sigma}_{\mathrm{p}}$ is obtained from the coarse grained polymer dynamics simulation. The polymeric stress $\boldsymbol{\sigma}_{\mathrm{p}}$ depends on the polymer chain conformation in the fluid particle.

2.1 Kernel Gradient Free Method

The original SPH method uses the following approximation for calculating the gradient of field variable:

$$\langle \boldsymbol{\nabla} f(\boldsymbol{x}) \rangle = \int \mathrm{d}\boldsymbol{x}' (\boldsymbol{\nabla}_{\boldsymbol{x}'} f(\boldsymbol{x}')) W \tag{7}$$

$$= \int \mathrm{d}\boldsymbol{S} f(\boldsymbol{x}') W - \int \mathrm{d}\boldsymbol{x}' f(\boldsymbol{x}') \boldsymbol{\nabla}_{\boldsymbol{x}'} W \tag{8}$$

$$\simeq \int \mathrm{d}\boldsymbol{x}' f(\boldsymbol{x}') \boldsymbol{\nabla}_{\boldsymbol{x}} W, \tag{9}$$

where $W = W(|\boldsymbol{x}' - \boldsymbol{x}|, h)$ is the kernel function interpolating fluid particles. From eq. (7) to eq. (9), we use the partial integral and the change of variables. The surface integral in eq. (8) is assumed to be zero because the kernel function is zero at the kernel boundary. When the fluid particles exist near the boundaries, e.g. the wall boundary or the free surface boundary, this assumption fails since the kernel boundary does not correspond to the boundary of integral. When the surface integral is not equal to zero, the original SPH method can not calculate the gradient of field variables accurately.

The kernel gradient free (KGF) method has succeeded in calculating the gradient of field variable accurately when the surface integral is not equal to zero. The KGF method is based on the Taylor expansion of field variable:

$$f(\boldsymbol{x}') = f(\boldsymbol{x}) + \boldsymbol{r} \cdot \boldsymbol{\nabla} f(\boldsymbol{x}) + \frac{1}{2} \boldsymbol{r}\boldsymbol{r} : \boldsymbol{\nabla}\boldsymbol{\nabla} f(\boldsymbol{x}) + O(|\boldsymbol{r}|^3), \tag{10}$$

where $\boldsymbol{r} = \boldsymbol{x}' - \boldsymbol{x}$. Multiplying $W(|\boldsymbol{r}|, h)$ to eq. (10) and integrating over $\boldsymbol{x}'$, we get

$$\int \mathrm{d}\boldsymbol{x}' f(\boldsymbol{x}') W = f(\boldsymbol{x}) \int \mathrm{d}\boldsymbol{x}' W + \boldsymbol{\nabla} f(\boldsymbol{x}) \cdot \int \mathrm{d}\boldsymbol{x}' \boldsymbol{r} W + \frac{1}{2} \boldsymbol{\nabla}\boldsymbol{\nabla} f(\boldsymbol{x}) : \int \mathrm{d}\boldsymbol{x}' \boldsymbol{r}\boldsymbol{r} W. \tag{11}$$

Substituting W to $\boldsymbol{r}W$ and $\boldsymbol{r}\boldsymbol{r}W$ in eq. (11), we get

$$\int \mathrm{d}\boldsymbol{x}' f(\boldsymbol{x}') \boldsymbol{r} W = f(\boldsymbol{x}) \int \mathrm{d}\boldsymbol{x}' \boldsymbol{r} W + \boldsymbol{\nabla} f(\boldsymbol{x}) \cdot \int \mathrm{d}\boldsymbol{x}' \boldsymbol{r}\boldsymbol{r} W + \frac{1}{2} \boldsymbol{\nabla}\boldsymbol{\nabla} f(\boldsymbol{x}) : \int \mathrm{d}\boldsymbol{x}' \boldsymbol{r}\boldsymbol{r}\boldsymbol{r} W, \tag{12}$$

and

$$\int \mathrm{d}\boldsymbol{x}' f(\boldsymbol{x}') \boldsymbol{r}\boldsymbol{r} W = f(\boldsymbol{x}) \int \mathrm{d}\boldsymbol{x}' \boldsymbol{r}\boldsymbol{r} W + \boldsymbol{\nabla} f(\boldsymbol{x}) \cdot \int \mathrm{d}\boldsymbol{x}' \boldsymbol{r}\boldsymbol{r}\boldsymbol{r} W + \frac{1}{2} \boldsymbol{\nabla}\boldsymbol{\nabla} f(\boldsymbol{x}) : \int \mathrm{d}\boldsymbol{x}' \boldsymbol{r}\boldsymbol{r}\boldsymbol{r}\boldsymbol{r} W. \tag{13}$$

The eqs. (11) - (13) can be summarized to matrix equation $\boldsymbol{A} \cdot \boldsymbol{X} = \boldsymbol{B}$;

$$\boldsymbol{A} = \begin{pmatrix} \langle 1 \rangle & \langle \boldsymbol{r} \rangle & \langle \boldsymbol{r}\boldsymbol{r} \rangle \\ \langle \boldsymbol{r} \rangle & \langle \boldsymbol{r}\boldsymbol{r} \rangle & \langle \boldsymbol{r}\boldsymbol{r}\boldsymbol{r} \rangle \\ \langle \boldsymbol{r}\boldsymbol{r} \rangle & \langle \boldsymbol{r}\boldsymbol{r}\boldsymbol{r} \rangle & \langle \boldsymbol{r}\boldsymbol{r}\boldsymbol{r}\boldsymbol{r} \rangle \end{pmatrix}, \tag{14}$$

$$\boldsymbol{X} = \begin{pmatrix} f \\ \boldsymbol{\nabla} f \\ \frac{1}{2} \boldsymbol{\nabla}\boldsymbol{\nabla} f \end{pmatrix}, \tag{15}$$

$$\boldsymbol{B} = \begin{pmatrix} \langle f \rangle \\ \langle \boldsymbol{r} f \rangle \\ \langle \boldsymbol{r}\boldsymbol{r} f \rangle \end{pmatrix}, \tag{16}$$

where $\langle O \rangle = \int \mathrm{d}\boldsymbol{x}' O(\boldsymbol{x}') W$. We can solve the matrix equation $\boldsymbol{A} \cdot \boldsymbol{X} = \boldsymbol{B}$ using LU decomposition and obtain $\boldsymbol{\nabla} f$ not $\langle \boldsymbol{\nabla} f \rangle$. Note that the kernel gradient $\boldsymbol{\nabla} W$ does not appear in eqs. (14) - (16). That is why this method is called as the kernel gradient free method.

In the simulation, $\langle O \rangle$ is computed using the following discrete form.

$$\langle O(\boldsymbol{x}_i) \rangle = \sum_{j \in \Omega_i} \frac{m_j}{\rho_j} O(\boldsymbol{x}_j) W(|\boldsymbol{x}_{ij}|, h), \quad (17)$$

$$\rho_i = \rho(\boldsymbol{x}_i) = \sum_{j \in \Omega_i} m_j W(|\boldsymbol{x}_{ij}|, h), \quad (18)$$

where Ω_i represents the cutoff region with the radius $2h$ from the i-th particle $\boldsymbol{x}_i$, and $\boldsymbol{x}_{ij} = \boldsymbol{x}_j - \boldsymbol{x}_i$.

2.2 Particle Shifting Method

When the fluid particles get closer, tensile instability occurs, where the particles make a string like structure and these strings repel each other [48]. The tensile instability affects the simulation results and should be suppressed. The pressure between the fluid particles does not disturb the tensile instability because the force acting on the fluid particles is the pressure gradient and the pressure gradient is zero between these close fluid particles. We need an extra trick to correct the particle positions to distribute uniformly.

The particle shifting method is one of the choices to suppress the tensile instability. The following direction vector $\boldsymbol{n}$ represents the direction of the nonuniform distribution of the fluid particles around $\boldsymbol{x}$.

$$\boldsymbol{n}(\boldsymbol{x}) = \int \mathrm{d}\boldsymbol{x}' \widehat{\boldsymbol{r}} W, \quad (19)$$

$$\widehat{\boldsymbol{r}} = \frac{\boldsymbol{r}}{|\boldsymbol{r}|}. \quad (20)$$

When we shift the particle at $\boldsymbol{x}$ to the direction $\boldsymbol{n}$, the particle distribution closes to uniform one. Using the direction vector $\boldsymbol{n}$, we define the shift vector $\Delta\boldsymbol{x}$:

$$\Delta\boldsymbol{x} = \epsilon \delta_0 \boldsymbol{n}, \quad (21)$$

where ϵ is the shift parameter. After the position and velocity of fluid particle is updated from $(\boldsymbol{x}_{\mathrm{old}}, \boldsymbol{v}_{\mathrm{old}})$ to $(\boldsymbol{x}^*, \boldsymbol{v}^*)$, according to (1) and (2), respectively, we apply the particle shifting method:

$$\boldsymbol{x}_{\mathrm{new}} = \boldsymbol{x}^* + \Delta\boldsymbol{x}, \quad (22)$$

$$\boldsymbol{v}_{\mathrm{new}} = \boldsymbol{v}^* + \Delta\boldsymbol{x} \cdot \boldsymbol{\nabla}\boldsymbol{v}. \quad (23)$$

Eq. (23) is obtained from the Taylor expansion of $\boldsymbol{v}(\boldsymbol{x} + \Delta\boldsymbol{x})$ around $\boldsymbol{x}$. When ϵ is less than 0.001, the tensile instability appears. On the other hand, when ϵ is larger than 0.1, the fluid particles make a crystalline structure and the dynamics of fluid particles shows stick-slip motion. The shift parameter ϵ should be set between 0.001 to 0.1.

2.3 Polymer Dynamics Simulation

The dynamics of entangled polymer chains is handled with the dual slip-link model. The dual slip-link model is placed on each fluid element and undergoes flow history that is nonuniform flow changing at each position and time.

In the dual slip-link model, the number of entanglements on a polymer chain in equilibrium state is proportional to the polymer chain length. The polymer chain with length L is separated to Z sub-vectors $\boldsymbol{r}_i, (i = 1, \cdots, Z)$ with unit length a representing the constraint tube between two entanglement points, or slip-links, and two free end segments s_1 and s_2: $L = s_1 + s_2 + \sum_{i=1}^{Z} |\boldsymbol{r}_i|$. Each slip-link has a pair of slip-link on the other polymer chain. The entangled polymer chain can move along the constraint tube.

When a shear flow applied to a chain, the tube segments are affinely deformed:

$$\frac{\mathrm{d}\boldsymbol{r}_i}{\mathrm{d}t} = \boldsymbol{\kappa} \cdot \boldsymbol{r}_i, \quad (24)$$

$$\boldsymbol{\kappa} = (\boldsymbol{\nabla}\boldsymbol{v})^{\mathrm{T}}, \quad (25)$$

where $\boldsymbol{\kappa}$ is obtained from the macroscopic fluid dynamics simulation. The length of polymer chain is assumed to follow the differential equa-

tion with Gaussian white noise $g_1(t)$:

$$\frac{\mathrm{d}L}{\mathrm{d}t} = -\frac{1}{\tau_\mathrm{R}}(L - L_0) + g_1(t) + \left(\frac{\mathrm{d}L}{\mathrm{d}t}\right)_\mathrm{affine}, \quad (26)$$

$$\tau_\mathrm{R} = \tau_0 Z^2, \quad (27)$$

$$L_0 = Z_0 a^2, \quad (28)$$

where τ_R is the Rouse relaxation time corresponding to the relaxation time of non-entangled polymer chain, τ_0 is the unit time of the slip-link model, L_0 is the equilibrium length. $\left(\frac{\mathrm{d}L}{\mathrm{d}t}\right)_\mathrm{affine}$ represents the difference of chain length between before and after affine deformation in eq. (24). The thermal fluctuation of polymer chain causes the center of mass motion along the tube segments. This is called as reptation. The reptation is achieved through updating the free end segments with Gaussian white nose $g_2(t)$:

$$\frac{\mathrm{d}s_1}{\mathrm{d}t} = \frac{1}{2}\left(\frac{\mathrm{d}L}{\mathrm{d}t}\right) + D_\mathrm{R} g_2(t), \quad (29)$$

$$\frac{\mathrm{d}s_2}{\mathrm{d}t} = \frac{1}{2}\left(\frac{\mathrm{d}L}{\mathrm{d}t}\right) - D_\mathrm{R} g_2(t), \quad (30)$$

where the first term represents the contribution from the chain difference from eq. (26) and the second term represents the reptation motion. $D_\mathrm{R} = \sqrt{2a^2/3\pi^2\tau_\mathrm{e} Z}$ is the diffusion constant of Rouse chain. Note that

$$\langle g_i(t)\rangle = 0, \quad (31)$$

$$\langle g_i(t) g_j(t')\rangle = \delta(t - t')\delta_{ij}. \quad (32)$$

When s_1 or s_2 is less than 0, the end of entanglement point and the pair of it disappear. On the other hand, when s_1 or s_2 is larger than a, the new entanglement point is created on the free end segment and the pair on the other polymer chain, selected randomly, are created. The stress tensor $\boldsymbol{\sigma}_\mathrm{p}$ is obtained from the dyadic of the tension of polymer chain and the direction of the tube segment averaging over the all chains in the fluid particle:

$$\boldsymbol{\sigma}_\mathrm{p} = G_0 \langle \sum_{i=1}^{Z} \frac{\boldsymbol{r}_i \boldsymbol{r}_i}{a|\boldsymbol{r}_i|} \rangle, \quad (33)$$

where $G_0 = (15/4)k_\mathrm{B}T/V$ is the unit shear modulus, k_B is the Boltzmann constant, T is the temperature, V is the unit volume.

2.4 Simulation Conditions

We consider 2-dimensional polymer melt flow around an cylindrical obstacle as same as the previous works [13, 15]. The cylinder with the radius R is made of particles fixed on the space. To disturb penetration of the fluid particles into the inside of the cylinder, the spaces between wall particles are smaller than δ_0. Since the density of the wall particles is higher than the bulk fluid, fluid particles are difficult to penetrate into the cylinder. At initial condition, fluid particles are placed at regular intervals with space δ_0 and polymer chains in the fluid particles are equilibrium states.

We impose the periodic boundary condition to the macroscopic system. The mass center of polymer chains in the microscopic system corresponds to the position of the macroscopic fluid particle. Since the polymer chains in the dual slip-link model are in the virtual space, we can ignore the diffusion of polymer chains between fluid particles.

We can obtain the zero-shear viscosity of dual slip-link model from the Green-Kubo formula.

$$\eta_\mathrm{p} = G_0^{-1} \int_0^\infty \mathrm{d}t \langle \sigma(t+\tau)\sigma(\tau)\rangle_\tau. \quad (34)$$

In the multiscale simulation, the zero-shear viscosity is modified to include the dissipation from the molecular vibration less than the tube:

$$\eta = \eta_\mathrm{p} + \eta_\mathrm{s}. \quad (35)$$

η_s represents the viscosity coming from the dissipation. We choose η as a characteristic viscosity in the multiscale simulation.

The time units of macroscopic simulation and microscopic simulation are set to the same. The velocity gradient obtained from the

macroscopic simulation is used to the microscopic simulation without any conversion factor. The stress unit of macroscopic simulation is normalized so that the characteristic viscosity η is equal to one.

Number of fluid particles in the system is 3,548 and each fluid particle has 1,000 polymer chains. Since the polymer simulators on each fluid particle are independent from the others, parallel computing is effective for the multiscale simulation. Using 3,456 cores on supercomputer systems at the SCC-ISSP for 24 hours, we can run the simulation sufficiently larger than the relaxation times of the short and long polymer chain melts.

We discuss the low Reynolds number flow where the flow around cylinder is expected to be symmetric. The Reynolds number is $\mathrm{Re} = \rho U R/\eta$ where ρ is the density of fluid, U is the maximum velocity of the flow, R is the radius of the cylinder, and η is the characteristic viscosity. Polymer melt has the relaxation time τ that the polymer chain stretch and orientation persist after cessation of applying the deformation. The polymer melt flow is characterized with the two dimensionless numbers, the Weissenberg number and the Deborah number. The Weissenberg number $\mathrm{Wi} = \tau\dot{\gamma}$ is the ratio of the viscous force and the elastic force. The Deborah number $\mathrm{De} = \tau/\tau_\mathrm{o} = \tau U/R$ is defined as the ratio of the relaxation time τ and the characteristic time scale of observation τ_o. We expect that the shear viscosity η_p decreases when the Weissenberg number is larger than one, and the non-symmetric flow field is observed when the Deborah number is larger than one.

3 Nonlinear Flow Behavior

We compare the results of a short polymer melt with $Z = 10$ and a long polymer melt with $Z = 20$. The relaxation time of $Z = 10$ is about 530 and that of $Z = 20$ is about 6400, obtained from the correlation function of the end-to-end

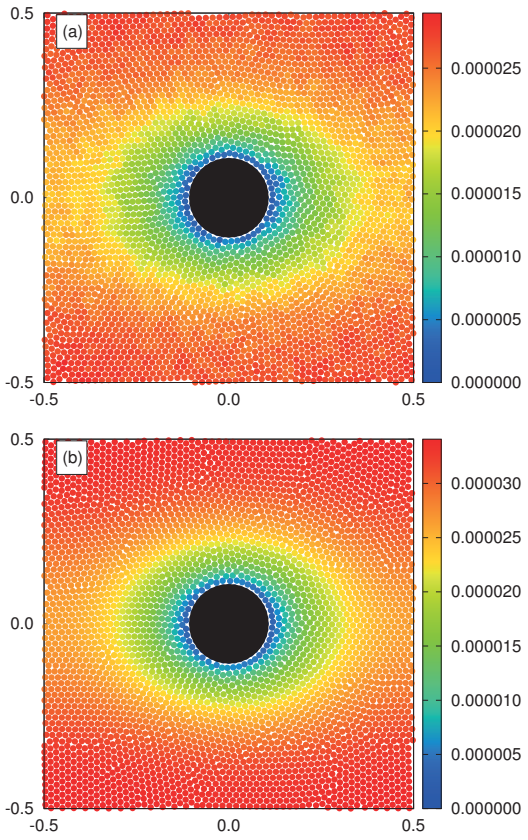

Figure 1: Velocity fields of (a) short chain melt and (b) long chain melt at steady state.

vector of polymer chain. The relaxation time of the long polymer melt is $2^{3.5}$ times larger than that of the short polymer melt. We use the normalized viscosity η and apply the same external force $\boldsymbol{g}$ to the fluid particles so that the Reynolds number is much less than one.

The velocity fields at steady state are summarized in Fig. 1. The Reynolds number is less than 0.1 in this condition. The maximum velocity of the long polymer melt is higher than that of the short polymer melt. We expect that the viscosity coming from the polymeric stress decreases in the long polymer melt because of the shear thinning phenomena.

The reason why the maximum velocity of the long chain melt is larger than that of the short chain melt will be found from comparing the stress tensors. Since each component of the stress tensor is not rotationally invariant, we obtain the eigen values and vectors of the

stress tensor, and compare them.

The largest eigen value and vector of the stress tensor are shown in Fig. 2 and Fig. 3, respectively. The eigen value field is almost symmetric among the upstream and downstream in the short polymer melt, while that is clearly not symmetric in the long polymer melt.

The asymmetry of the eigen value field is coming from the Deborah number. The Deborah number is higher than one in the long polymer melt and is less than one in the short polymer melt. The eigen vectors both in the short and long polymer melts are aligned to the same direction in the vicinity of the cylinder where the Weissenberg number is larger than one. In the short polymer melt, however, the orientation is random away from the cylinder where the Weissenberg number is less than one. Polymers are extended and aligned in the long polymer melt rather than the short polymer melt, resulting in the shear thinning phenomena.

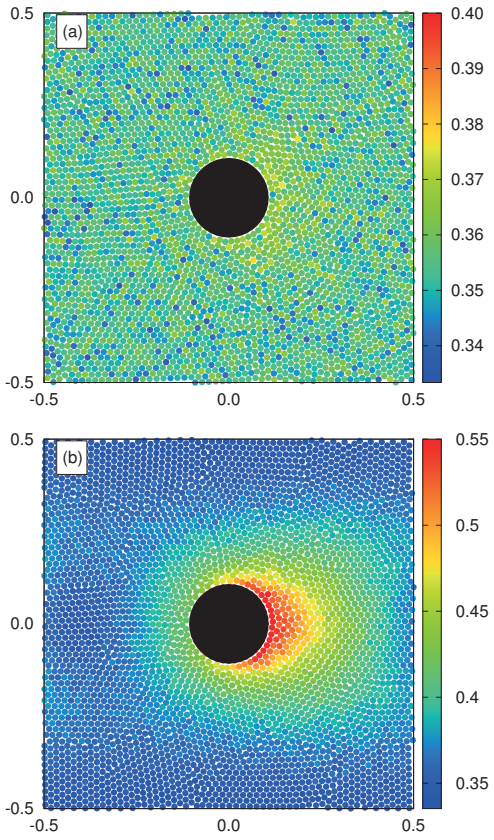

Figure 2: The largest eigen values of the stress tensor of (a) short chain melt and (b) long chain melt at steady state.

4 Summary

We have reviewed the multiscale simulation that is composed of the fluid particle simulation and the polymer dynamics simulation. The fluid particle simulation has been solved using the kernel gradient free method and the particle shifting method. These two methods stabilize the fluid particle simulation. The dual slip-link model has been used as the polymer dynamics simulation in the multiscale simulation. This model has a full chain picture and can treat the entanglement between the polymer chains. We have shown a flow around a cylinder in cases of the short and long polymer melts. The long polymer melt has shown the shear thinning phenomena while the short polymer melt has not. The asymmetric fields of the largest eigen value and the corresponding eigen vector of the stress tensor have suggested the polymer chain stretch and orientation around the obstacle. Especially in the long polymer chain melt, the asymmetry is clear because the relaxation time or the correlation time of the long polymer chain melt is $2^{3.5}$ times longer than that of the short polymer chain melt.

To decrease the noise, the number of polymer chains in the polymer dynamics simulation should be increased from the point of view of the central limit theorem in probability theory. We have developed the ensemble average method using several replica simulation boxes for a fluid particle to obtain the stress tensor averaging over the replica [49]. This method needs 10 to 100 times larger super computer than that we used here and has been only applied to one dimensional problem. We will apply the noise reduction technique to the multiscale simulation of two or three dimensional problem in the future using a super computer

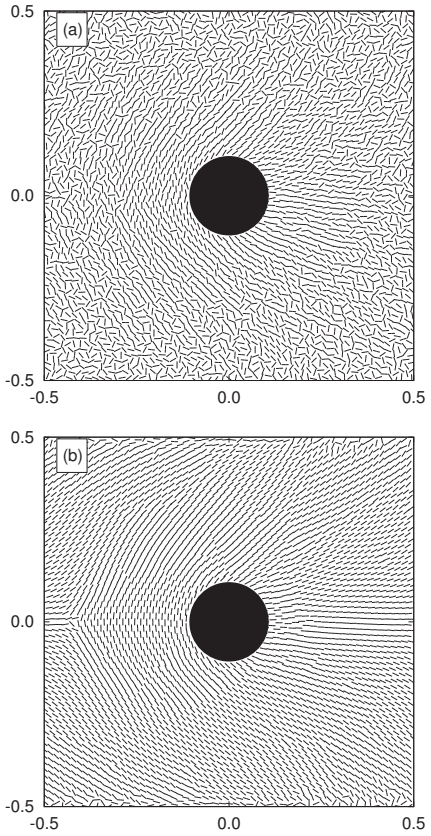

Figure 3: The eigen vectors (corresponding to Fig. 2) of the stress tensor of (a) short chain melt and (b) long chain melt at steady state.

with more than 1,000,000 cores.

Acknowledgment

This work was supported by JSPS KAKENHI Grant Number 15K17733. The computation in this work was done using the facilities of the Supercomputer Center, Institute for Solid State Physics, University of Tokyo.

References

[1] C. W. Macosko, "*Rheology*", Wiley-VCH, Inc. (1994).

[2] R. G. Larson, "*The Structure and Rheology of Complex Fluids*", Oxford University Press (1999).

[3] R. G. Owens and T. N. Phillips, "*Computational Rheology*", Imperial College Press (2002).

[4] M. Laso and H. C. Ottinger, J. Non-Newtonian Fluid Mech., **47** (1993) 1.

[5] H. K. Rasmussen and O. Hassager, J. Non-Newtonian Fluid Mech., **56** (1995) 65.

[6] H. A. Hulsen et al., J. Non-Newtonian Fluid Mech., **70** (1997) 79.

[7] P. Halin et al., J. Non-Newtonian Fluid Mech., **79** (1998) 387.

[8] A. P. G. van Heel et al., J. Rheol., **43** (1999) 1239.

[9] E. A. J. F. Peters et al., J. Rheol, **44** (2000) 811.

[10] H. A. Hulsen et al., J. Non-Newtonian Fluid Mech., **98** (2001) 201.

[11] C. C. Hua and J. D. Schieber, J. Rheol., **42** (1998) 477.

[12] T. Murashima and T. Taniguchi, J. Polym. Sci. B, **48** (2010) 886.

[13] T. Murashima and T. Taniguchi, Europhys. Lett., **96** (2011) 18002.

[14] T. Murashima and T. Taniguchi, J. Phys. Soc. Jpn., **81** (2012) SA013.

[15] T. Murashima et al., J. Phys. Soc. Jpn., **82** (2013) 012001.

[16] W. Ren and W. E, J. Comp. Phys., **204** (2005) 1.

[17] S. De et al., Phys. Rev. E, **81** (2010) 030801(R).

[18] S. Yasuda and R. Yamamoto, Phys. Fluid., **20** (2008) 113101.

[19] S. Yasuda and R. Yamamoto, Europhys. Lett., **86** (2009) 18002.

[20] S. Yasuda and R. Yamamoto, Phys. Rev. E, **81** (2010) 036308.

[21] W. E, "*Principles of Multiscale Modeling*", Cambridge University Press (2011).

[22] J. J. Monaghan, Rep. Prog. Phys., **68** (2005) 1703.

[23] M. Ellero et al., J. Non-Newtonian Fluid Mech., **105** (2002) 35.

[24] M. Ellero and R. I. Tanner, J. Non-Newtonian Fluid Mech., **132** (2005) 61.

[25] J. Fang et al., J. Non-Newtonian Fluid Mech., **139** (2006) 68.

[26] X.-J. Fan et al., J. Non-Newtonian Fluid Mech., **165** (2010) 219.

[27] H. Zhu et al., J. Non-Newtonian Fluid Mech., **165** (2010) 362.

[28] T. Jiang et al., Appl. Math. Model., **35** (2011) 3833.

[29] J. K. Chen et al., Comput. Mech., **23** (1999) 279.

[30] J. K. Chen et al., Comput. Mech., **24** (1999) 273.

[31] G. M. Zhang and R. C. Batra, Comp. Mech., **34** (2004) 137.

[32] M. B. Liu et al., Appl. Math. Model., **29** (2005) 1252.

[33] C. Huang et al., Int. J. Numer. Meth. Fluids, **78** (2015) 691.

[34] R. Xu et al., J. Comp. Phys., **228** (2009) 6703.

[35] K. Kremer and G. Grest, **92** (1990) 5057.

[36] P. G. de Gennes, J. Chem. Phys., **55** (1971) 572.

[37] M. Doi and S. F. Edwards, "The Theory of Polymer Dynamics", Oxford University Press, (1986).

[38] G. Marrucci, J. Non-Newtonian Fluid Mech., **62** (1996) 279.

[39] G. Ianniruberto and G. Marrucci, J. Non-Newtonian Fluid Mech., **65** (1996) 241.

[40] D. W. Mead et al., Macromol., **31** (1998) 7895.

[41] C. C. Hua and J. D. Schieber, J. Chem. Phys., **109** (1998) 10018.

[42] J. T. Padding and W. J. Briels, J. Chem. Phys., **115** (2001) 2846.

[43] Y. Masubuchi et al., J. Chem. Phys., **115** (2001) 4387.

[44] M. Doi and J. Takimoto, Phyl. Trans. R. Soc. Long. A, **361** (2003) 641.

[45] A. E. Likhtman, Macromol., **38** (2005) 6128.

[46] R. Khaliullin and J. Schieber, Macromol., **42** (2009) 7504.

[47] T. Uneyama, J. Soc. Rheol. Jpn. (Nihon Reoroji Gakkaishi), **39** (2011) 135.

[48] J. P. Morris, arxiv:astro-ph/9503124 (1995) (unpublished).

[49] T. Murashima et al., AIP Conf. Proc., **1518** (2013) 436.